discharge rates are required. Figure 4B shows that IE-Li($Ni_{0.5}Mn_{0.5}$)O_2 clearly retains its energy storage capacity even at the very high rate required for those applications. At a 6-min charge/discharge rate, IE-Li($Ni_{0.5}Mn_{0.5}$)O_2 delivers almost double the energy density of SS-Li($Ni_{0.5}Mn_{0.5}$)O_2. Initial tests on the capacity retention with full charge/discharge cycling are promising, with a fade of 0.6% per cycle for IE-Li($Ni_{0.5}Mn_{0.5}$)O_2 versus 0.8% per cycle for SS-Li($Ni_{0.5}Mn_{0.5}$)O_2 (*17*).

In conclusion, we have used ab initio computational modeling to infer that the combined use of low-valent transition-metal cations and low strain in the activated state are key strategies for increasing the rate capability of layered cathode materials, and we have successfully synthesized Li($Ni_{0.5}Mn_{0.5}$)O_2 with very little intralayer disordering to optimize those factors. In agreement with our theoretical predictions, this material retains its capacity at high rates. Substitution of Co for Ni and Mn can also be used to reduce the Li/Ni exchange and improve rate performance (*23*, *24*), although the use of Co increases the cost and reduces the safety of the material (*25*). Although Li($Ni_{0.5}Mn_{0.5}$)O_2 displays an exciting combination of high rate and high capacity, several other factors, such as thermal stability, cycle life, and the extra cost from the ion-exchange process, will need to be further investigated before its application in commercial products can be considered. If the outcome of such development studies is positive, Li($Ni_{0.5}Mn_{0.5}$)O_2 would be a potential cathode material for high rate applications.

References and Notes

1. M. S. Whittingham, *Science* **192**, 1126 (1976).
2. A. Van der Ven, G. Ceder, *Electrochem. Solid-State Lett.* **3**, 301 (2000).
3. A. Van der Ven, G. Ceder, *J. Power Sources* **97-98**, 529 (2001).
4. T. Ohzuku, Y. Makimura, *Chem. Lett. (Jpn.)* **8**, 744 (2001).
5. Z. Lu, D. D. MacNeil, J. R. Dahn, *Electrochem. Solid-State Lett.* **4**, A191 (2001).
6. J. Reed, G. Ceder, *Electrochem. Solid-State Lett.* **5**, A145 (2002).
7. J. M. Paulsen, J. R. Dahn, *J. Electrochem. Soc.* **147**, 2478 (2000).
8. M. M. Thackeray, *Prog. Solid State Chem.* **25**, 1 (1997).
9. Y. Makimura, T. Ohzuku, *J. Power Sources* **119-121**, 156 (2003).
10. Z. Lu, L. Y. Beaulieu, R. A. Donaberger, C. L. Thomas, J. R. Dahn, *J. Electrochem. Soc.* **149**, A778 (2002).
11. C. Delmas *et al.*, *J. Power Sources* **68**, 120 (1997).
12. M. S. Whittingham, U.S. Pat. 4,007,055 (1975).
13. E. J. Wu, P. D. Tepesch, G. Ceder, *Philos. Mag. B* **77**, 1039 (1998).
14. A. R. Armstrong, P. G. Bruce, *Nature* **381**, 499 (1996).
15. C. Delmas, J. J. Braconnier, A. Maazaz, P. Hagenmuleer, *Rev. Chimie Minérale* **19**, 343 (1982).
16. K. Kang *et al.*, *Chem. Mater.* **15**, 4503 (2003).
17. Materials and methods are available as supporting material on *Science* Online.
18. Y. S. Meng *et al.*, *Chem. Mater.* **17**, 2386 (2005).
19. H. Kobayashi *et al.*, *J. Mater. Chem.* **13**, 590 (2003).
20. W. S. Yoon *et al.*, *Electrochem. Solid-State Lett.* **5**, A263 (2002).
21. C. P. Grey, W. S. Yoon, J. Reed, G. Ceder, *Electrochem. Solid-State Lett.* **7**, A290 (2004).
22. C. Delmas *et al.*, *Int. J. Inorg. Mater.* **1**, 11 (1999).
23. Z. Lu, D. D. MacNeil, J. R. Dahn, *Electrochem. Solid-State Lett.* **4**, A200 (2001).
24. T. Ohzuku, Y. Makimura, *Chem. Lett. (Jpn.)* **7**, 642 (2001).
25. J. Jiang, K. W. Eberman, L. J. Krause, J. R. Dahn, *J. Electrochem. Soc.* **152**, A1879 (2005).

26. The authors would like to thank Y. Shao-Horn for valuable discussion. This work was supported by the Materials Research Science and Engineering Centers program of the National Science Foundation under award DMR 02-13282 and by the Assistant Secretary for Energy Efficiency and Renewable Energy, Office of FreedomCAR and Vehicle Technologies of the U.S. Department of Energy under contract DE-AC03-76SF00098, subcontracts 6517748 and 6517749, with the Lawrence Berkeley National Laboratory.

Supporting Online Material

www.sciencemag.org/cgi/content/full/311/5763/977/DC1
Materials and Methods
Figs. S1 to S4
References

2 November 2005; accepted 20 January 2006
10.1126/science.1122152

Plasma Acceleration Above Martian Magnetic Anomalies

R. Lundin,[1] D. Winningham,[2] S. Barabash,[1] R. Frahm,[2] M. Holmström,[1] J.-A. Sauvaud,[3] A. Fedorov,[3] K. Asamura,[4] A. J. Coates,[5] Y. Soobiah,[5] K. C. Hsieh,[6] M. Grande,[7] H. Koskinen,[8,9] E. Kallio,[8] J. Kozyra,[10] J. Woch,[11] M. Fraenz,[11] D. Brain,[12] J. Luhmann,[12] S. McKenna-Lawler,[13] R. S. Orsini,[14] P. Brandt,[15] P. Wurz[16]

Auroras are caused by accelerated charged particles precipitating along magnetic field lines into a planetary atmosphere, the auroral brightness being roughly proportional to the precipitating particle energy flux. The Analyzer of Space Plasma and Energetic Atoms experiment on the Mars Express spacecraft has made a detailed study of acceleration processes on the nightside of Mars. We observed accelerated electrons and ions in the deep nightside high-altitude region of Mars that map geographically to interface/cleft regions associated with martian crustal magnetization regions. By integrating electron and ion acceleration energy down to the upper atmosphere, we saw energy fluxes in the range of 1 to 50 milliwatts per square meter per second. These conditions are similar to those producing bright discrete auroras above Earth. Discrete auroras at Mars are therefore expected to be associated with plasma acceleration in diverging magnetic flux tubes above crustal magnetization regions, the auroras being distributed geographically in a complex pattern by the many multipole magnetic field lines extending into space.

Earth's polar aurora and related phenomena, such as magnetic and ionospheric disturbances, have been studied for well over half a century. The first proof that the aurora is caused by energetic electrons precipitating into Earth's topside atmosphere came from high-altitude sounding-rocket measurements (*1*). Electrons accelerated downward by magnetic field–aligned electric fields cause intense bright auroral arcs, often referred to as discrete auroras. Intense fluxes of nearly monoenergetic electrons (*2*) were the first evidence for magnetic field–aligned electric fields. Subsequent observations of accelerated electrons were made from polar orbiting satellites. The electrons' peak energy displayed a characteristic "inverted-V" signature in an energy-time spectrogram (*3*), which became the particle attribute of a discrete aurora. An additional proof of concept was observations of electrons and ions accelerated in opposite directions (*4*, *5*).

Inverted-V–like ion features near Mars, first reported by the Phobos-2 spacecraft (*6*), were associated with the temporal and spatial variability of the energy and momentum transfer between martian plasma and the solar wind (*7*, *8*). This was because auroras, specifically discrete auroras, are associated with magnetized planets, and no strong intrinsic magnetic fields were evident from Phobos-2 data, thus ruling out any analogy with the terrestrial aurora.

The Mars Global Surveyor (MGS) findings of crustal magnetic anomalies at Mars (*9*) considerably changed the picture. We now expect to find diverging magnetic field "cusps" above Mars (*10*) and closed magnetic loops (*11*), with local magnetic conditions similar to those found above Earth's polar region, albeit weaker and topologically different. A set of magnetic multipoles at specific longitudes and latitudes of Mars may characterize the crustal magnetization. Indeed, the first observation of auroral emission at Mars (*12*) was made above a strong crustal magnetization at 177°E and 52°S. The emissions in the 150- to 300-nm bands (CO and O) were most likely excited by high fluxes of charged particles.

Our study identified regions with downward-accelerated electrons and upward-accelerated ionospheric ions near local midnight. We studied how the acceleration regions map to magnetic cusps and clefts bound by strong magnetizations at Mars. We compared the energy spectra of accelerated electrons in the nightside of Mars with those associated with terrestrial discrete auroras. Finally, we computed the energy flux of precipitating electrons and estimated, from a

terrestrial analogy, the expected intensity of the nightside aurora at Mars.

The Analyzer of Space Plasma and Energetic Atoms (ASPERA-3) experiment (*13*) has two plasma instruments: an Eectron Spectrometer (ELS) and an Ion Mass Analyzer (IMA). The ELS provides electron measurements in the energy range from 0.001 to 20 keV, with 8% energy resolution. The intrinsic field of view is 4° × 360°. The 360° aperture is divided into 16 sectors.

The IMA provides ion measurements in the energy range from 0.01 to 30 keV for the main ion components H^+, He^{++}, He^+, and O^+ and for the group of molecular ions [$20 < M/q < \sim 80$ (M, mass; q, electric charge)]. The IMA has a 4.6° × 360° field of view. Electrostatic sweeping provides elevation (±45°) coverage for a total field of view of about 2π.

ASPERA-3 data from 33 Mars Express (MEX) traversals of the martian cavity were analyzed, most of the data being taken during a period of favorable eclipse orbits in February and March 2005. During this period, the spacecraft traversed the midnight-sector cavity. An important selection criterion was the acceleration of ions and electrons; the ionospheric ions accelerated upward and the electrons accelerated downward. The spacecraft "footprint" was mapped in geographic latitude and longitude down to a 400-km MGS "open-closed" magnetic field map.

During an inverted-V event on 20 February 2005 (Fig. 1), narrow beams of heavy ions [O^+ (30%), O_2^+ (49%), and CO_2^+ (21%)], consistent with the ionospheric composition at 220 to 250 km (*14*), were observed to flow upward/tailward while substantial fluxes of electrons moved in the opposite direction (downward/sunward). Displaced Maxwellian distributions were used for temperature calculations (that is, the temperatures were determined from the high-energy tail of the electron and ion distributions). The beams are relatively cool (Fig. 1), the beam energy being substantially higher than the thermal energy. The general characteristics of these inverted-V events are (i) the coincident existence of narrow upgoing ionospheric ion beams and energized downgoing electrons and (ii) a tendency for the downward electron acceleration to increase with decreasing altitude. These are characteristics analogous to those of auroral acceleration near Earth. The trajectory in fact maps to semi-open magnetic field lines: in the boundary between a magnetic anomaly and open field lines. It does not map

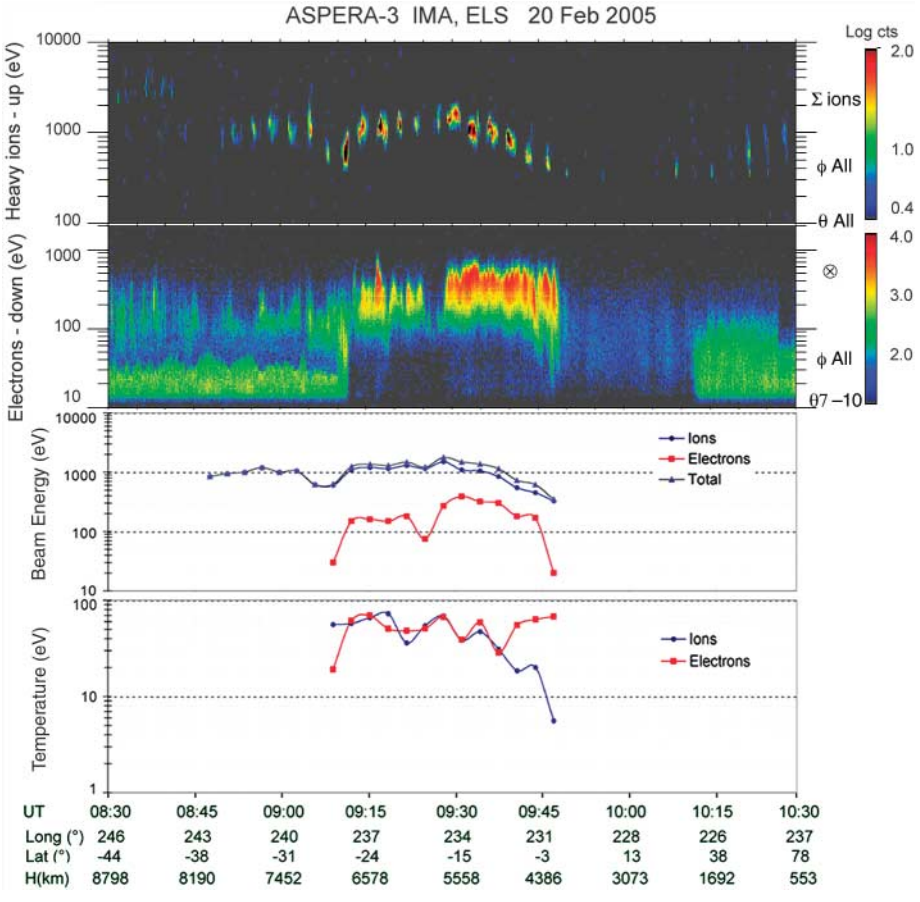

Fig. 1. Energy-time spectrogram for ions and electrons during an inverted-V event in the tail eclipse. The third panel from the top shows the acceleration energy (peak energy) and total acceleration (electrons + ions). The bottom panel shows electron and ion temperatures. Coordinates are Mars east longitude and latitude. UT, universal time; H, height.

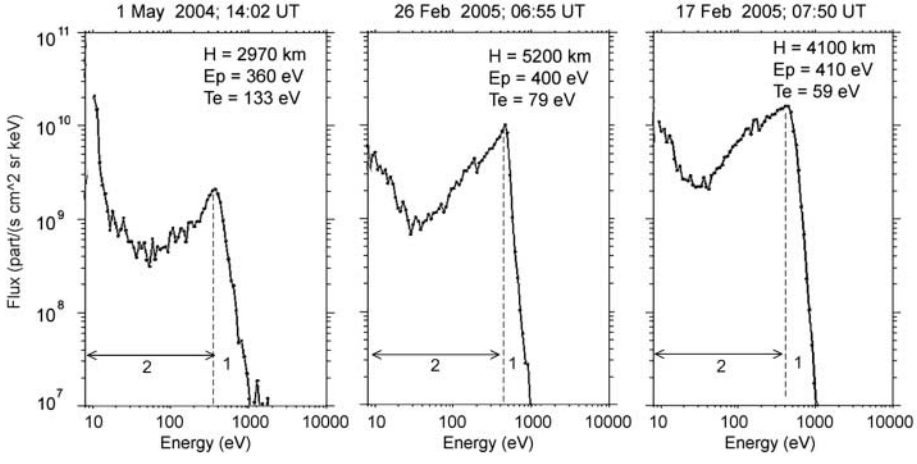

Fig. 2. Three ASPERA-ELS electron energy spectra taken at different altitudes and times, suggesting acceleration through a potential drop V_0 ($E_p = eV_0$). Te, electron temperature. The energy regimes correspond to accelerated primaries (1) and backscattered + secondary electrons (2).

[1]Swedish Institute of Space Physics, Box 812, S-98 128, Kiruna, Sweden. [2]Southwest Research Institute, San Antonio, TX 7228–0510, USA. [3]Centre d'Etude Spatiale des Rayonnements, BP-4346, F-31028 Toulouse, France. [4]Institute of Space and Astronautical Science, 3-1-1 Yoshinodai, Sagamichara, Japan. [5]Mullard Space Science Laboratories, University College London, Surrey RH5 6NT, UK. [6]Department of Space Physics, University of Arizona, Tucson, AZ 85721, USA. [7]Rutherford Appleton Laboratory, Chilton, Didcot, Oxfordshire OX11 0QX, UK. [8]Finnish Meteorological Institute, Box 503 FIN-00101 Helsinki, Finland. [9]Department of Physical Sciences, University of Helsinki, Helsinki, Finland. [10]Space Physics Research Laboratory, University of Michigan, Ann Arbor, MI 48109–2143, USA. [11]Max-Planck-Institut für Sonnensystemforschung, D-37191 Katlenburg-Lindau, Germany. [12]Space Science Laboratory, University of California, Berkeley, CA 94720–7450, USA. [13]Space Technology Ltd., National University of Ireland, Maynooth, County Kildare, Ireland. [14]Instituto di Fisica dello Spazio Interplanetari, I-00133 Rome, Italy. [15]Applied Physics Laboratory, Johns Hopkins University, Laurel, MD 20723–6099, USA. [16]Physikalisches Institut, University of Bern, CH-3012 Bern, Switzerland.

directly to the closed flux-tube magnetic anomaly. This is another analogy with Earth's auroral zone: The inverted V's are usually found in the boundary region between open and closed magnetic field lines.

Three ELS electron spectra from three separate orbits (Fig. 2) provide further evidence for auroral acceleration in a quasi-static electric potential drop. Based on an acceleration model (*15*), the characteristics of downward/parallel acceleration of electrons in a potential drop V_0 can be identified: a sharp energy peak, E_p, related to accelerated primary electrons ($E_p = eV_0$), and secondary electrons originating from reflection and backscattering above Mars. Upgoing ions form narrow monoenergetic beams; the downgoing electrons are more isotropic and less monoenergetic. These characteristics are consistent with theory (*16*) and observations (*5*) near Earth.

A good correlation is seen between ion beam energy and ion beam temperature (Fig. 3, left). The linear relation $y = 8.5x + 623$ (eV) has a correlation coefficient $R^2 = 0.76$. Studies of upward-flowing H^+ ions near Earth by the Viking satellite [figure 2.28 of (*5*)] give a similar linear relation $y = 4.9x + 210$ (eV), with $R^2 = 0.74$. The relations imply that ion heating goes together with parallel acceleration. The ion beams are cool below ≈1 keV, with the temperature increasing proportional to the parallel energy above ≈1 keV, but the beam energy remains at least a factor of 10 higher than the beam temperature. In analogy with Earth, the increased ion beam temperature may be due to a transverse (to the magnetic field) acceleration process (*17*). The electron beam energy and electron thermal energy (Fig. 3, right) also appear to be correlated, although with less significance ($R^2 = 0.58$) than the ion correlation. Electron temperatures for low-energy peaks are in the range typical for the magnetosheath (20 to 50 eV). Wave activity inferred from high-time resolution ELS data in connection with ion and electron heating (*18*, *19*) suggests that waves are the cause of the gradual electron heating.

A statistical analysis of the maximum ion inverted-V peak energy shows no altitude dependence ($R^2 = 0.15$). This implies that the acceleration process is quite variable, governed by external solar wind dynamics (pressure and interplanetary electric and magnetic fields). As for the mapping of the acceleration regions to magnetic anomalies, we find a tendency for inverted V's to occur near local midnight, the observations clustering around the mean 162°E and –7°S. The clustering of observations close to local midnight is in part due to the selection criteria (the cavity).

When the inverted-V footprints are plotted versus geographic latitude and longitude, an interesting picture emerges (Fig. 4): a clustering of data points in boundaries between open and closed field lines. Few data points fall within larger areas of open (red) or closed (black) magnetic field. We therefore conclude that the

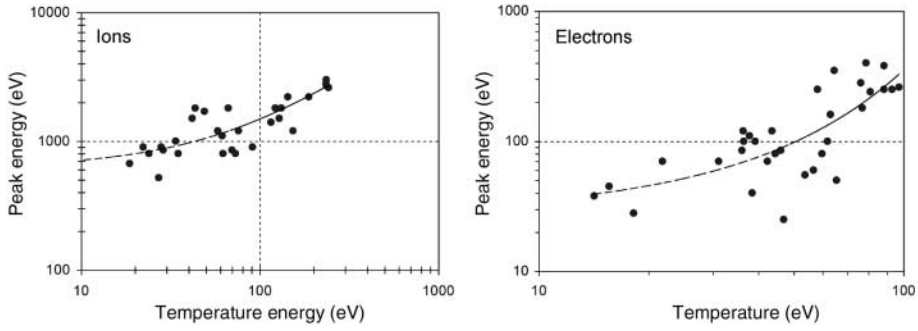

Fig. 3. Ion and electron inverted-V peak energy versus temperature in the nightside of Mars. (**Left**) Ions. The dashed line marks a linear fit with function $y = 8.5x + 623$ (eV), $R^2 = 0.76$. (**Right**) Electrons. The dashed line marks an exponential fit with function $y = 27.2 \cdot \exp(0.026x)$ (eV). $R^2 = 0.58$.

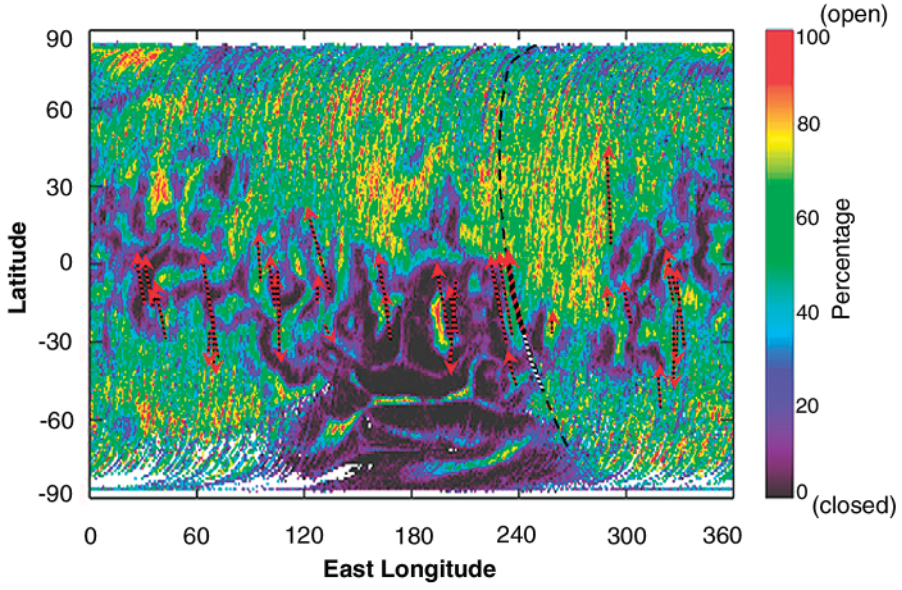

Fig. 4. Satellite ground track projections of nightside ion inverted V's and their relation to crustal magnetization. The scale at right indicates the percentage of open magnetic field lines at MGS altitudes (≈400 km), with red indicating 100% open and black 100% closed magnetic flux tubes. The satellite ground tracks are indicated by dashed lines; the red arrowheads mark the exit of the inverted V's. The black dashed line near longitude 240° marks the entire ground track of the inverted-V traversal shown in Fig. 1.

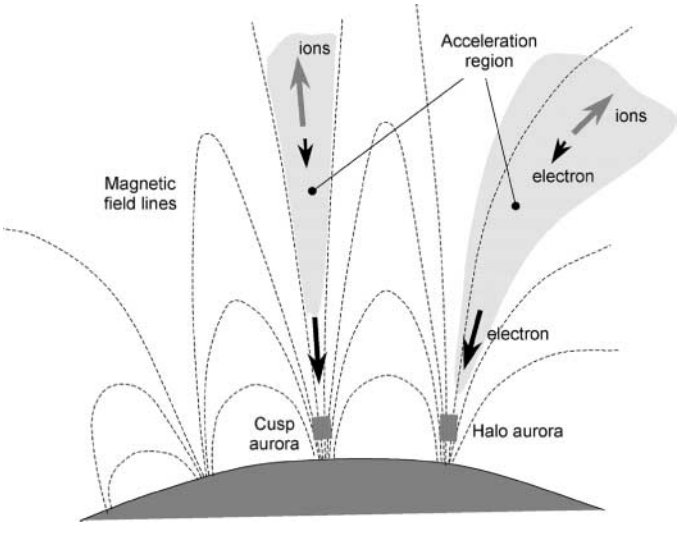

Fig. 5. Diagram of the auroral plasma acceleration above the magnetic anomalies at Mars. A cusp/cleft aurora is expected to occur between adjacent anomalies and a halo aurora to occur circumscribing the large-scale region of crustal magnetization.

inverted V's are associated with boundary regions between open and closed field lines. The precipitation of electrons and the corresponding acceleration and escape of ionospheric ions take place in clefts interfacing magnetic anomalies and in the boundary interfacing the large-scale magnetization region with the nonmagnetized region at Mars.

Results from ASPERA-3 on MEX (*20*) suggest that energization and outflow of plasma may initiate at fairly low altitudes. Similarly, the nightside energization and outflow may also reach down to low altitudes, perhaps even lower in view of the low nightside ionization. The observations of upward-accelerated ions combined with downward-accelerated electrons are observed on flux tubes that are semi-open or open, connecting to strong crustal magnetizations. However, we also observe acceleration in boundaries enclosing the large-scale regions of crustal magnetization. The intense fluxes of upgoing ionospheric ions represent the erosion of ionospheric plasma and the formation of plasma density cavities (*21*). A combination of parallel electric fields and waves deepens the cavities and promotes an acceleration process in which parallel acceleration and heating are strongly coupled. This is consistent with the linear relation found between the ion peak/beam energy and the beam temperature (Fig. 3, left), as previously observed above terrestrial discrete auroras associated with field-aligned plasma acceleration (*5*).

Discrete auroras are therefore expected to occur in clefts interfacing with strong crustal magnetization regions at Mars (Fig. 5), but also in the interface region connecting the void and presence of crustal magnetizations at Mars. To complete the analogy between terrestrial discrete auroras and martian auroras, the precipitating energy flux of electrons Θ_a is derived by adding the local energy flux Θ_i and the energy flux gained by electron acceleration P_a down to the atmosphere. P_a is computed using the acceleration voltage (V_0) inferred from upgoing ionospheric ion beams (Fig. 3, left). For electrostatic acceleration along a unit magnetic flux tube, assuming acceleration in a narrow altitude range, the total energy flux gain is given by $P_a \approx eV_0\Phi_i$, where Φ_i represents the local downward electron flux. Thus $\Theta_a \approx \Theta_i + eV_0\Phi_i$. From 17 inverted V's, we obtain the local maximum energy flux Θ_i = 0.01 to 3 mW/m^2, from which we derive Θ_a = 1 to 50 mW/m^2. The latter corresponds to 2- to 80-kilorayleigh visible emissions (at 557.7 nm; the "green line") above Earth. In a similar manner, the density distribution of atomic oxygen from a time-averaged model of the martian atmosphere (*22*) suggests that the green-line aurora is generated above magnetic cusps and clefts in the nightside of Mars at atmospheric heights of 50 to 80 km.

References and Notes

1. C. E. MacIlwain, *J. Geophys. Res.* **65**, 2727 (1961).
2. R. D. Albert, *Phys. Rev. Lett.* **18**, 368 (1967).
3. L. A. Frank, K. L. Ackerson, *J. Geophys. Res.* **76**, 3612 (1971).
4. E. G. Shelley, R. G. Johnson, R. D. Sharp, *Geophys. Res. Lett.* **3**, 654 (1976).
5. T. E. Moore *et al.*, *Space Sci. Rev.* **88**, 7 (1999).
6. R. Lundin *et al.*, *Nature* **341**, 609 (1989).
7. H. Pérez-de Tejada, *J. Geophys. Res.* **92**, 4713 (1987).
8. J. G. Luhmann, S. J. Bauer, *AGU Monogr.*, **66**, 417 (1992).
9. M. J. Acuña *et al.*, *Science* **284**, 790 (1999).
10. A. M. Krymskii *et al.*, *J. Geophys. Res.* **107** (A9), 1245 (2002).
11. D. L. Mitchell *et al.*, *J. Geophys. Res.* **106**, 23419 (2001).
12. J.-L. Bertaux *et al.*, *Nature* **435**, 9 (2005).
13. S. Barabash *et al.*, in *Mars Express: The Scientific Payload* (ESA SP-1240, European Space Agency, Noordwijk, Netherlands, 2004), pp. 121–139.
14. W. B. Hanson *et al.*, *J. Geophys. Res.* **82**, 4351 (1977).
15. D. S. Evans, *J. Geophys. Res.* **79**, 2853 (1974).
16. Y. T. Chiu, M. Schulz, *J. Geophys. Res.* **83**, 629 (1978).
17. R. D. Sharp, R. G. Johnson, E. G. Shelley, *J. Geophys. Res.* **82**, 3324 (1977).
18. J. D. Winningham *et al.*, *Icarus,* in press.
19. R. Lundin *et al.*, *Icarus,* in press.
20. R. Lundin *et al.*, *Science* **305**, 1933 (2004).
21. W. Calvert, *Geophys. Res. Lett.* **8**, 919 (1981).
22. M. B. McElroy *et al.*, *J. Geophys. Res.* **82**, 4379 (1977).

23. ASPERA-3 on the European Space Agency's (ESA's) MEX is a joint effort between 15 laboratories in 10 countries. We are indebted to the national agencies supporting ASPERA-3 and to ESA for making MEX a great success.

31 October 2005; accepted 5 January 2006
10.1126/science.1122071

Dissociation of $MgSiO_3$ in the Cores of Gas Giants and Terrestrial Exoplanets

Koichiro Umemoto,[1] Renata M. Wentzcovitch,[1]* Philip B. Allen[2]

$CaIrO_3$-type $MgSiO_3$ is the planet-forming silicate stable at pressures and temperatures beyond those of Earth's core-mantle boundary. First-principles quasiharmonic free-energy computations show that this mineral should dissociate into CsCl-type MgO + cotunnite-type SiO_2 at pressures and temperatures expected to occur in the cores of the gas giants and in terrestrial exoplanets. At ~10 megabars and ~10,000 kelvin, cotunnite-type SiO_2 should have thermally activated electron carriers and thus electrical conductivity close to metallic values. Electrons will give a large contribution to thermal conductivity, and electronic damping will suppress radiative heat transport.

The transformation of $MgSiO_3$-perovskite into the $CaIrO_3$-type structure near Earth's core-mantle boundary (CMB) conditions (*1–3*) invites a new question: What is the next polymorph of $MgSiO_3$? The importance of this question has increased since the discoveries of two new exoplanets: the Earth-like planet with ~7 Earth masses (*4*) (Super-Earth hereafter) and the Saturn-like planet with a massive dense core with ~67 Earth masses (*5*) (Dense-Saturn hereafter). The extreme conditions at the giants' cores (*6*) and exoplanet interiors are challenging for first-principles methods. Electrons are thermally excited, and core electrons start to participate in chemical bonds. This requires either all-electron methods or the development of pseudopotentials based on core orbitals. Neither density functional theory (DFT) nor the quasiharmonic approximation (QHA) have been tested at these ultrahigh pressures and temperatures (*PT*s). Here, we use the Mermin functional (*7*), i.e., the finite electronic temperature (T_{el}) version of DFT that includes thermal electronic excitations, and ultrasoft pseudopotentials (*8*) based on orbitals with quantum number n = 2 and 3 for all three atoms. We studied $MgSiO_3$, MgO, and SiO_2 up to 80 Mbar and 20,000 K (figs. S1 and S2, A to C).

$MgSiO_3$ could transform to another ABX_3-type silicate or dissociate. We searched systematically for possible ABX_3 structures having likely high-pressure coordinations and connectivities, but found none with enthalpy lower than the $CaIrO_3$-type polymorph (see supporting online material). This phase dissociated into CsCl-type MgO and cotunnite-type SiO_2 at 11.2 Mbar in static calculations (Fig. 1). Both binary oxides undergo phase transitions below 11.2 Mbar. MgO undergoes the NaCl-type → CsCl-type transformation at 5.3 Mbar, and SiO_2 undergoes a series of phase transitions: stishovite → $CaCl_2$-type → α-PbO_2-type → pyrite-type → cotunnite-type at 0.48, 0.82, 1.9, and 6.9 Mbar, respectively (Fig. 2). Our static transition pressures agree well with previous first-principles results (*9–12*) and experimental transition pressures (*13*, *14*), except for the α-PbO_2-type → pyrite-type transition in SiO_2, which has been observed once at 2.6 Mbar (*15*). CsCl-type MgO and cotunnite-type SiO_2 have not yet been seen experimentally. Baddeleyite-type and OI-type phases occur as pre-cotunnite phases in TiO_2 (*16*), an analog of SiO_2. Our results show

[1]Department of Chemical Engineering and Materials Science and Minnesota Supercomputing Institute, University of Minnesota, 421 Washington Avenue SE, Minneapolis, MN 55455, USA. [2]Department of Physics and Astronomy, Stony Brook University, Stony Brook, NY 11794–3800, USA.

*To whom correspondence should be addressed. E-mail: wentzcov@cems.umn.edu